Article citation info:
Li Z. Detection research of telecentric bright field imaging system based on multi-angle illumination in ultra-precision machining components. Diagnostyka. 2025;26(1):2025101. https://doi.org/10.29354/diag/197234.

DIAGNOSTYKA, 2025, Vol. 26, No. 1

e-ISSN 2449-5220
DOI: 10.29354/diag/197234

DETECTION RESEARCH OF TELECENTRIC BRIGHT FIELD IMAGING SYSTEM BASED ON MULTI-ANGLE ILLUMINATION IN ULTRA-PRECISION MACHINING COMPONENTS

Zhuolin LI

Moral Education • Integrated Teaching and Research Training Department,
Jilin Provincial Institute of Education, Changchun, 130000, China
Corresponding author, e-mail: zhuolin77772023@163.com

Abstract

Due to the rapid development of industrial automation and intelligence, the performance requirements of the machine vision inspection system are increased, especially for the surface of components with different properties. Firstly, the detection of single-sided polished optical element surface based on coaxial incidence telecentric bright field imaging system is proposed, and the upper and lower surfaces with different properties are compared. Secondly, the gray value change of defect location is distinguished, and then different scratch defect information is extracted. Finally, the detection data of the sample is calculated, and the weak information extraction algorithm based on visual difference excitation and double discrete the Fourier Transform is proposed. The average diameter of the sample is 6109.50 pixels, the average nominal value is 101.60 mm, the scratch pixel length and width are 184 pixels and 7.23 pixels respectively, and the actual length and width are 3.06 mm and 0.12 mm, respectively. The experimental results show that the detection technology of weak defects on the surface of single-sided polished optical elements can realize the nondestructive automatic quantitative detection of sapphire substrate, and can provide theoretical reference and technical support for the development of intelligent industrial applications.

Keywords: component surface properties, bright field imaging, visual differential excitation, the Fourier transform, defect segmentation.

1. INTRODUCTION

Due to the in-depth promotion of the development of national "scientific and technological innovation", the manufacturing quality and quality detection of ultra-precision machined components in the industry and even national defense applications need to be more rigorous and accurate. Machine vision inspection technology is more important for automated monitoring and quality control in the industrial manufacturing industry. It is used for automatic detection of product surface defects in industries such as automobiles, mechanical manufacturing, shipbuilding, and aerospace to ensure the high-quality requirements of manufactured products 1. However, the widely used manual visual inspection has the problems of strong subjectivity, low efficiency, and low accuracy, which has been unable to meet the development goals of modern automation and intelligence. In particular, the detection of weak defect images is prone to lead to missed detection of machine detection. Scholars at home and abroad have discussed the object and technology of defect detection, including the detection method of metal surface defects using an active red thermal external imaging system [2-3], the recognition method based on the gated recursive unit network for nondestructive detection of defects [4], and the improved method of visual inspection model combined with transfer learning to detect the surface defects of wind turbine blades [5]. Based on this research, the algorithm of visual differential excitation and double discrete the Fourier Transform (VDEDDFT) is established by using a telecentric bright field imaging system, visual differential excitation technology, and the Fourier Transform, aiming to realize the nondestructive automatic quantitative detection of sapphire substrate, it also provides technical reference for the development of ultra-precision component testing and automation industry.

The first part is to elaborate and summarize the current detection system and related applications. In the second part, the telecentric bright field imaging system is used to analyze the surface properties of single-sided polished optical elements to understand the characteristics of defect information extraction

Received 2024-04-11; Accepted 2024-12-11; Available online 2025-01-06

and enhancement. The third part is to compare the gray value of the defect texture attributes and extract the information fine by combining the Fourier Transform algorithm and the visual difference image. The fourth part is a summary and description of the whole study.

2. RELATED WORKS

In the development of industrial automation and national defense application research, the development of ultra-precision machining components and its detection technology is closely related to the machine vision detection technology, especially for the weak scratch defects on the surface of ultra-precision machining components with different attributes, the machine detection technology and detection performance need to be strengthened and improved. In recent years, scholars at home and abroad have done a lot of research on weak defect detection technology of components. Duan et al. proposed to use principal component analysis and support vector machine to build a monitoring model for identifying defects on the surface of continuous casting slabs, thus obtaining the superior detection performance of the model [6]. Kang et al. proposed the use of ultrasonic and sensor detection methods for wind turbine blade surface defect detection, thus proving the effectiveness of this method [7]. Hua et al. proposed a laser vision detection method based on model segmentation for the detection of vehicle body surface defects, thus proving its strong robustness and high detection rate [8]. According to the surface defects of different objects, the nondestructive testing technology is studied, and the models of different methods are constructed, so as to obtain higher recognition and detection performance. However, it is widely used in metal surface defect detection, and different methods are used to build the detection model. Preeyanka et al. proposed to use the Fourier Transform infrared spectroscopy for the detection of quantum dots and metal ions, so as to improve the detection rate of the system [9]. Ai et al. proposed the use of ultrasonic and infrared thermal imaging technology for metal surface defects, so as to improve the performance and feasibility of the detection technology [10]. Zhao et al. proposed to use you only live once (YOLOv4) structure and feature pyramid module to improve the accuracy of the algorithm for metal surface defect detection, thus proving the high recognition accuracy of the model [11].

Build algorithms and models on defect images in other fields to enhance image information or detect and locate methods. Yu et al. proposed to use the improved differential formula to identify the defect image for the problem of building defect image recognition, thus indicating the high performance of the recognition method [12]. Aydin et al. proposed a model integrating a deep learning algorithm for the classification of railway track defects to locate the rail, thus proving the high accuracy of the model [13]. Wang et al. proposed using a convolutional neural network and principal component analysis to build a model of aluminum foil surface defects, thus proving the superiority of the defect detection performance of the model [14]. In the production and testing of battery quality, defect detection technology is widely used, and the methods of different material properties are different. Zhuang et al. proposed a convolution method based on multi-component attention for surface defect detection on the problem of color difference recognition of solar cells, thus proving the high performance and high detection rate of the model [15]. Zachman et al. proposed a centroid scanning transmission electron microscope for imaging detection of battery materials to enhance imaging, which has the advantages of detection and imaging [16]. Chen et al. proposed the use of a visual detection algorithm and robot detection technology for the quality inspection of lithium batteries to detect the surface defects of batteries, thus proving the high performance of the algorithm [17]. Danjuma et al. proposed the use of prediction technology for the solar photovoltaic system to enhance efficiency, so as to improve the availability of the system [18]. Rabha et al. proposed to use the built-in camera to build three dynamic adaptive imaging modes for the imaging of smart phones, thus proving the wide application of the mode [19]. Lu et al. proposed the use of quantitative phase microscopy and mixed bright and dark fields for intensity transmission, thus proving the effectiveness of their method [20]. Chen et al. proposed the reconstruction lens mode for photon imaging to punish the correction entropy, so as to improve the feasibility of the imaging system [21]. Schrimpf et al. proposed the use of pipe lens detection to improve the accuracy of droplet size for field measurement technology, thus proving the effectiveness of the system [22]. In addition, the detection technology and image imaging system are also applied in smart phones or field monitoring, and good results and development have been achieved.

In summary, although domestic and foreign scholars have established many models and algorithms for surface defect technology of different objects and imaging technology in other fields, there is very little experimental data applied to ultra-precision machining components, and it is widely used in single experimental objects. Therefore, research has innovatively adopted weak defect detection technology and combined it with coaxial incidence far-centered bright field imaging system, disparity excitation algorithm, and the Fourier Transform to form a new angle of object surface defect detection technology method, proving its high recognition and detection rate.

3. OPTICAL ELEMENT SURFACE DEFECT DETECTION TECHNOLOGY

Aiming at the problem of missing detection of weak defects on the surface of machined

components and optical components, the detection algorithm and the technical analysis of the detection system based on telecentric bright field imaging and visual difference excitation are studied. The single-sided polished optical components are used, and the surface characteristics of their upper and lower attributes and the receiving effect of different lenses on light are analyzed, so as to design a coaxial incident and telecentric bright field imaging method (CITBFI) based on coaxial incidence, and design a VDEDDFT algorithm affected by the diffuse light from the lower surface.

3.1. Optical elements with single-sided polished surface properties analysis

The upper and lower surfaces of single-sided polished optical surfaces (SSPOS) have different properties, in which the upper surface is super smooth and the lower surface is frosted unpolished. Specific examples are as follows: a single-sided polished sapphire substrate, the upper surface of which is a substrate grown by the semiconductor material gallium nitride (GaN), and its quality will affect the epitaxial growth of GaN and the performance of the finished product. The most important factor affecting the quality is the surface scratch defect, which will increase the occurrence of dislocation in the epitaxial layer and expand the stress between the wafer and the epitaxial layer [23]. For the detection of SSPOS scratch defects, the effects of dark field detection and bright field detection should be compared respectively, as shown in Fig. 1.

It can be seen from Fig. 1 that (a) is the attribute characteristics of the upper and lower surfaces of SSPOS, and (b) is the dark field detection method of SSPOS. The incident light passes through the super smooth surface and generates reflected light in different directions on the frosted lower surface. After passing through the super smooth surface, the diffuse reflected light enters the imaging system together with the scattered light of the defect, so that the defect and the background cannot be identified together. (c) is a transmission-type bright field detection method. After the vertical incident light passes through the frosted surface the light becomes diffuse light and diffuse light is emitted at the smooth position of the defect on the upper surface, so that the defect cannot be identified if the contrast cannot be formed at the defect position. Therefore, when using the machine vision detection system of the super smooth surface to detect the defect position of single-sided polished optical elements, it cannot meet the formation and recognition of gray contrast. Because the lower surface of SSPOS will destroy the dark field detection method, a defect detection system for distinguishing the upper and lower surfaces of SSPOS is designed by using the bright field detection method, so as to analyze the different angles of the upper and lower surfaces to the incident light and the angle of the system imaging light. First, the upper and lower surfaces are illuminated by the normal incidence light angle, and the vertical reflected light is formed at the smooth part of the upper surface, the scattered light is formed at the defect, and the diffuse reflected light is formed at the lower surface. Then the imaging system is selected to analyze the three kinds of light, as shown in Fig. 2.

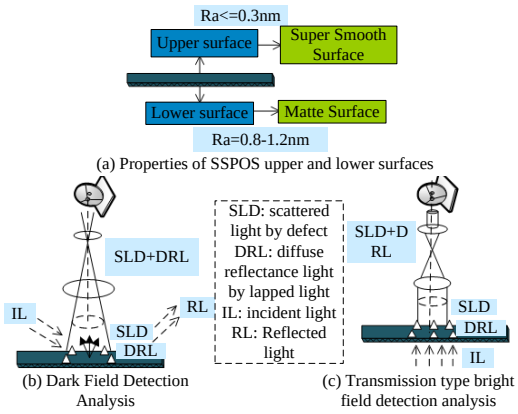

Fig. 1. SSPOS indicators attributes and dark and bright field detection

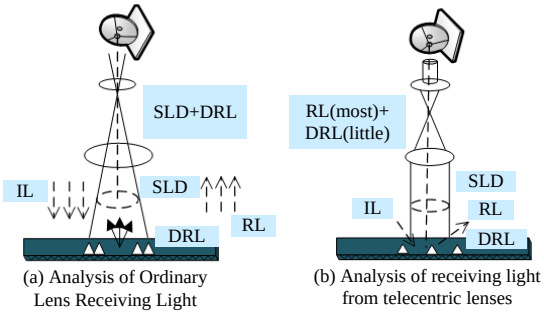

Fig. 2. Analysis of different imaging rays in different lenses

In Fig. 2, it is found that (a) shows the reception analysis of light by the ordinary lens, which can receive all the vertically reflected light from the smooth surface, but some scattered light at the defect is missing, and the gray contrast of the defect location is poor, and it is covered by the bright background; (b) shows the detection of telecentric lens. It is found that the smooth surface of the imaging display is a bright background, and the gray level of the defect location is dark. However, due to the arbitrariness of the diffuse light on the lower surface, only a few defect information is received, and there is still a certain gray level difference between the defect information and the background. The surface scratch defects can be regarded as weak defects. Under the influence of the diffuse light from the lower surface, the contrast of the defects displayed by the machine vision imaging system is low, and it will also be affected by the surrounding background and texture. According to the characteristics of different imaging systems, the CITBFI system is designed. However, in order to solve the problem of low gray contrast between the

scratch defect image and the background image, it is necessary to analyze the characteristics of the defect location image from the three-dimensional distribution of the gray image, as shown in Fig. 3.

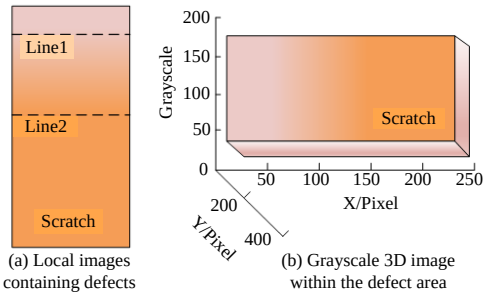

(a) Local images containing defects

(b) Grayscale 3D image within the defect area

Fig. 3. Grayscale changes of surface defects in coaxial incident far field imaging

From Fig. 3 (a), it is found that although the gray level changes of the defect location can be retained in the CITBFI imaging, the particle information on the lower surface will also produce gray level changes and affect the image background; The human visual system can find the defect information instead. The scratches on SSPOS are vertically illuminated by parallel incident light, while the telecentric lens receives different light rays from the surface of the component, thereby displaying the area and grayscale features of the scratches in the imaging system. In the displayed component surface image, the contrast between the scratch defect image and the background image is relatively low. Therefore, a grayscale feature comparison is performed on the image to distinguish between the scratch defect image and the background image. In Fig. 3 (b), different information of the image is processed based on the visual system characteristics of the human eye, including defect texture and transformation domain, to remove interference information and retain effective defect images.

3.2. Telecentric bright field imaging system and visual differential excitation algorithm

The system can retain the weak defect information in the image in the form of a gray jump, but it will also retain the information of fine particles on the lower surface and uneven illumination image, which constitute a complex image. The visual features of human eyes are used to enhance the contrast of defect texture information and remove the interference of uneven background, in which there is no need to carry out special operations on the uneven background and noise of the image. Visual subtraction technology can enhance the grayscale pattern of images, thereby enhancing the defect features of images, and improving the recognition speed and accuracy of detection models. The difference excitation operator of the image can simulate the texture structure operator with the divergence and saliency characteristics of human eyes, and then calculate the saliency change of the image. The difference excitation operator formula is shown in Eq. (1).

$$C = \frac{\Delta I}{S} \tag{1}$$

In Eq. (1), S represents the intensity of the initial image stimulus, ΔI is the incremental threshold of image change, C is the ratio that remains constant on the right side of the formula, and the ratio of $\frac{\Delta I}{S}$ is the Weber score. The local salient features are extracted from the difference excitation image, and the background fluctuations are removed to enhance the weak features of the scratch defects in the image. However, the local saliency feature can be represented by the gray value changes of the central pixel and adjacent pixels. First, the sum of the gray differences is calculated between the current pixel and the neighboring pixels, as shown in Eq. (2).

$$V_{sum} = \sum_{i=0}^{p-1}(\Delta x_i) = \sum_{i=0}^{p-1}(x_i - x_c) \tag{2}$$

In Eq. (2), $x_i\,(i = 0,1,...p-1)$ represents the i neighborhood pixel of the current pixel x_c, p is the number of neighborhood pixels. Secondly, the ratio is calculated between the sum of the gray difference and the gray level of the current pixel, as shown in Eq. (3).

$$D_{ratio}(x_c) = \frac{V_{sum}}{x_c} \tag{3}$$

In Eq. (3), D_{ratio} is the difference ratio, and then its arctangent function is taken as the difference excitation of the current pixel, as shown in Eq. (4).

$$\vartheta'(x_c) = \arctan\left[\frac{V_{sum}}{x_c}\right] = \arctan\left[\sum_{i=-0}^{p-1}\left(\frac{x_i - x_c}{x_c}\right)\right] \tag{4}$$

In Eq. (4), arctan is an arctangent function, which can limit the rapid increase or decrease of the output value due to the change of the input value, and the result value can maintain the difference information, rather than the absolute value. If $\vartheta(x_c)$ is positive, the brightness of the surrounding pixel is lower than that of the central pixel; On the contrary, if $\vartheta(x_c)$ is negative, the brightness is high. To reduce the interference of image background brightness change on defect information, as shown in Eq. (5).

$$\vartheta'(x_c) = \arctan\left[\sum_{i=-0}^{p-1}\left(\frac{A\times(x_i + a) - A\times(x_c + a)}{A\times(x_c + a)}\right)\right] \tag{5}$$

In Eq. (5), A and a represent the interference constant of the pixel by the background brightness, that is, the multiplicative background change and the additive background change. Finally, the differential excitation image is calculated as shown in Eq. (6).

$$I_2 = 255\times\frac{\vartheta - \vartheta_{\min}}{\vartheta_{\max} - \vartheta_{\min}} \tag{6}$$

In Eq. (6), the difference excitation value of the original image is normalized to the gray-scale image of $[0,255]$, and stretched within its range to observe the change of gray-scale value between pixels in the difference excitation image. Calculating the difference excitation image can obtain the significant features of gray changes and reduce the background interference, so as to enhance the defect information of the original image, but also enhance the particle details and image noise of the lower surface of SSPOS. Because the scratch defect texture has a certain directionality, it is necessary to consider the texture features of different information to segment the defect texture. The calculated difference excitation value cannot segment the defect texture information, but the scratch has linear characteristics and irregular detail texture. Different texture features are used to recognize the linear defect texture in the difference excitation image. The commonly used method for detecting line features is the Hough transform, which uses polar coordinates of lines and accumulators to extract pixels on the same line in the image. First, assume the line parameters and formulas, and then take two points from the line and meet the parameter formula, as shown in Eq. (7).

$$\begin{cases} x\cos\varphi + y\sin\varphi = \varepsilon \\ x_1\cos\varphi + y_1\sin\varphi = \varepsilon \\ x_2\cos\varphi + y_2\sin\varphi = \varepsilon \end{cases} \tag{7}$$

In Eq. (7), (ε,φ) is the parameter of the linear formula, and the two points are respectively $A(x_1,y_1)$ and $B(x_2,y_2)$. If the coordinate system is transformed into a formula (ε,φ), the intersection point on its corresponding curve is the parameter of the corresponding straight-line formula.

3.3. Defect detection algorithm based on double discrete the Fourier transform

The scratch pixels of the same line cannot be detected, and then consider analyzing the directionality of texture performance, and analyze the difference of frequency size and frequency directionality of different textures in the frequency domain. First, assume that the size of the difference excitation image is m × n. The direction of the texture image is parallel to the X-axis, as shown in Eq. (8).

$$\begin{cases} f(x,y) = f(x) \\ f(x,y) = f(x)\times f(y), f(y) = 1 \end{cases} \tag{8}$$

In Eq. (8), $f(x,y)$ is a texture image, and its gray level does not change with the y position. Then the Fourier Transform is performed, as shown in Eq. (9).

$$F(u,v) = \frac{1}{m\times n}\sum_{x=0}^{m-1}\sum_{y=0}^{n-1} f(x,y)\exp\left[-j2\pi\left(\frac{xu}{m}+\frac{yv}{n}\right)\right] = F(u)\times F(v) \tag{9}$$

In Eq. (9), $F(u,v)$ represents the Fourier Transform; Then the parameter simplification process is carried out to obtain the Fourier Transform result of the scratch image, as shown in Eq. (10).

$$F(u,v) = \begin{cases} F(u), & v = 0 \\ 0, & other \end{cases} \tag{10}$$

In Eq. (10), the Fourier spectrum energy of the texture image in the vertical direction $v = 0$ and parallel y direction is concentrated here. According to the property of the Fourier Transform, the energy of the spectral image of the scratch texture obtained by the Fourier Transform is concentrated in the direction perpendicular to the scratch. The spectrum image corresponding to the scratch is extracted, and then the scratch defect image is segmented from the original image by the Fourier Transform. At present, the machine vision inspection system is based on the visual mode of human eyes observing defects, and extracts the effective defect information of the image based on the digital image, so as to calculate the defect parameters to evaluate the quality of the tested samples, as shown in Fig. 4.

From Fig. 4, it is found that the detection of surface defects in the machine vision system includes image acquisition, image processing, and image feedback. According to the above principles and methods, a surface weak defect extraction algorithm based on visual difference excitation and double discrete the Fourier Transform is designed, as shown in Fig. 5.

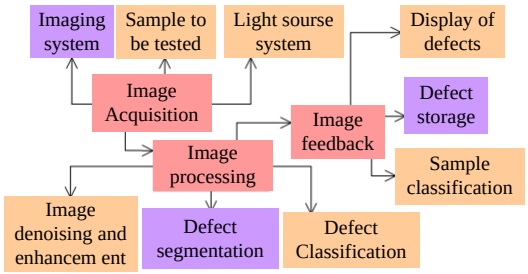

Fig. 4. Machine vision system composition for surface defect detection

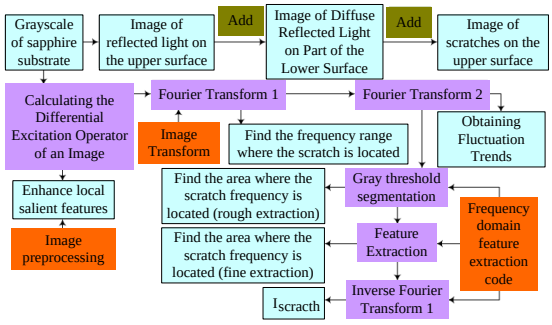

Fig. 5. Surface defect extraction algorithm based on visual differential excitation and double discrete the Fourier Transform

It is found from Fig. 5 that the VDEDDF algorithm is mainly composed of visual difference excitation operation and double the Fourier

Transform. CITBFI system is used to collect the sapphire substrate image, including the image of reflected light on the upper surface, the image of partial diffuse light on the lower surface, and the image of scratch on the upper surface; Firstly, the difference excitation operator of the image is calculated to enhance the local salient features; Secondly, the frequency and fluctuation trend of scratch were obtained by the Fourier Transform; Then, the gray threshold is segmented to extract the scratch frequency region, and the fine feature is extracted; Finally, inverse the Fourier Transform is used to obtain the scratch defect image 23. The high gray area and low gray area that appear according to the background fluctuation represent that there are high gray information and low gray information in the image at this time. In order to distinguish the two kinds of information, the gray threshold segmentation method is used, as shown in Eq. (11).

$$\begin{cases} \alpha_{low} = \dfrac{1}{N_{low}} \times \sum\limits_{(x,y)\in I_{4-low}} I_{4-low}(x,y) \\ \alpha_{high} = \dfrac{1}{N_{high}} \times \sum\limits_{(x,y)\in I_{4-high}} I_{4-high}(x,y) \end{cases} \tag{11}$$

In Eq. (11), I_{4-high} and I_{4-low} respectively represent high gray level information and low gray level information, and the number of pixels is N_{high} and N_{low}, respectively, α_{high} and α_{low} are the average value of the pixel set. The variance of the two is calculated as shown in Eq. (12).

$$\delta(Threshold) = N_{low}(Th) \times N_{high}(Th) \times \left[\alpha_{low}(Th) - \alpha_{high}(Th)\right]^2 \tag{12}$$

In Eq. (12), $\delta(Threshold)$ represents the selected threshold, and its range is $[0,255]$. The best gray segmentation threshold can be obtained when the calculated variance is the maximum. From the segmented scratch image, the length and width of the scratch are calculated to obtain its geometric pixel characteristics, so as to calculate the actual size of the scratch. The actual length of the scratch and the number of image pixels are approximately linear inertia, and the ratio of the two is calculated as shown in Eq. (13).

$$L = K_L \times L_{pixel} \tag{13}$$

In Eq. (13), L is the actual length of the scratch, L_{pixel} is the pixel length of the scratch image, and K_L is the ratio constant of the two. The scratch width needs to be calculated by the total area of scratch pixels, as shown in Eq. (14) and (15).

$$W_{pixel} = \frac{S_{pixel}}{L_{pixel}} \tag{14}$$

In Eq. (14), W_{pixel} represents the average width of scratch pixels and S_{pixel} is the area of scratch pixels.

$$S_{pixel} = sum\left(Scratch_{pixel}\right) \tag{15}$$

In Eq. (15), $Scratch_{pixel}$ is the sum of scratch pixels. Using the defect image established after inversing the Fourier Transform, the binary image of the scratch is extracted by using binarization and line detection, and the actual size of the scratch defect is obtained. Sapphire substrates are usually subjected to quality testing using extremely high-temperature annealing technology to enhance their hardness, brittleness, and corrosion resistance, thereby providing a technical basis for the reprocessing and use of substrate materials, and thus providing reliability in material performance in the manufacturing industry 23.

4. COMPONENT SURFACE DEFECT DETECTION ALGORITHM AND SYSTEM IMAGING ANALYSIS

The CITBFI system mainly consists of a front mirror group, a color separation filter, and a rear mirror group. The color separation filter makes the incident light received by the object consistent with the incident angle. The incident surface is equipped with a color separation film, which has a high imaging effect on the detection image. The total pixel count of the imaging chip is 1920 × 1920, the total diagonal length is 11mm, and the effective imaging area is 9.216 × 9.216mm. And the study used a white light scanning interference microscope with a system stand size of 1 × 1m-2 × 2m, the core is based on the NewView 7000 series of ZYGO, which has a wide and precise range for measuring samples, with a resolution of up to 0.1nm. The size of the sapphire substrate used in the CITBFI system is 2 inches and 4 inches, and the maximum diameter of the test sample is 102mm. The detection field set by the system, namely the field of view of the telecentric imaging lens, is 130mm, while the pixel size of each line in the linear array camera is 8192 pixels, and the image resolution is 16um. As shown in Fig. 6.

From Fig. 6, it can be seen that the machine components of the 4-inch sapphire substrate and telecentric imaging lens are arranged according to the bright field detection method. The lens is located above the device and can be selected according to different experiments. Sapphire, as an epitaxial layer growth substrate for gallium nitride materials, plays an important role in material fabrication and performance requirements due to its surface quality. Due to the high hardness, brittleness, and stable chemical properties of sapphire, its ultra-precision machining poses significant challenges. Therefore, in order to achieve the surface quality of single-sided polishing, high-precision and high-efficiency polishing of sapphire substrate substrates is carried out using single-sided grinding machines and flat polishing techniques. Combined with the high-quality requirements of semiconductor material gallium nitride, the surface roughness of sapphire after polishing is below 0.3nm, while the roughness

of the other frosted surface is between 0.8-1.2nm. Studying the detection of scratch defects on sapphire substrates can also provide technical support for subsequent material fabrication.

a)

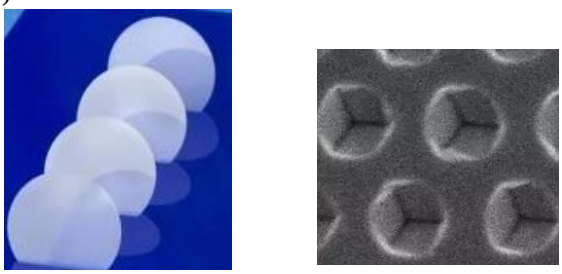

b)

Fig. 6. Image and apparatus of the experimental setup: a) apphire substrate and detection images, b) telecentric imaging lens device and components

Research on defect detection technology for optical component surfaces, using single-sided polished optical component surfaces, i.e. sapphire substrate substrates, and conducting imaging system analysis on their surface scratches. Firstly, the study combines the CITBFI system to perform bright field detection on the surface of components, and saves images based on different lighting conditions on the surface of the components. Secondly, the contrast between surface scratch images and background information is poor under lens imaging, making it difficult to accurately detect the defect information of components. Finally, the VDEDDF algorithm is used to segment, deepen texture, and extract features from scratch information in the image, in order to segment defect information from the original image and improve the detection technology of component surface defects. According to the defect image analysis collected by the CITBFI system, the gray level of the scratch defect image was improved, and the gray level of the background image had a certain fluctuation; Compared with the gray jump of the surrounding background, the gray jump of the defective pixel was not obvious, and then compared with the gray change of the defect and the background area, as shown in Fig. 7.

From Fig. 7 (a), it was found that the grayscale jump amplitude of non-defect positions was relatively significant, and their grayscale values are all above 100 as the pixel increases. However, in Fig.

a)

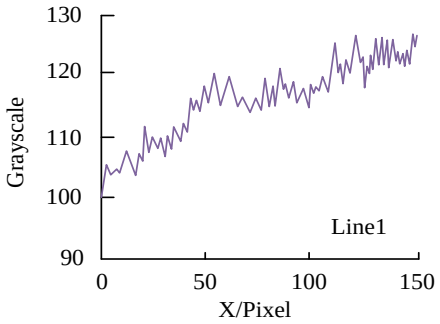

b)

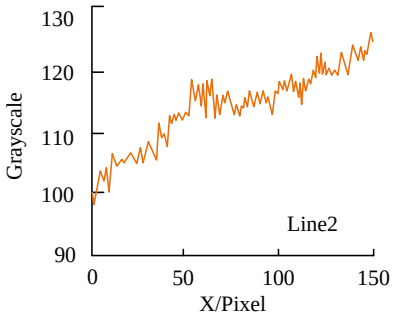

Fig. 7. Grayscale changes of defects and background: a) excluding grayscale changes in defect areas, b) including grayscale changes in defect areas

7 (b), the grayscale jump amplitude of defect positions was smaller than that of non-defect positions, indicating that human vision was more likely to detect defects. Therefore, complex image information was processed based on human visual features, interference information was removed, and effective defect images were preserved and enhanced. A weak defect extraction algorithm based on visual differential excitation and double discrete the Fourier Transform was proposed. In order to enhance the texture information of defects and distinguish background information, the Hough line detection method was used to detect and calculate the scratch pixels and surrounding background information on the defect image, as shown in Fig. 8.

From Fig. 8 (a), it is found that the upper part of the straight line is the parameter abscissa, and the lower part is the parameter ordinate; The blue curve in Fig. 8 (b) is a sine curve and intersects with the orange curve as a point P. However, due to the similarity of the differential excitation value between the defect background and the surrounding background in the differential excitation image, the Hough transform method cannot detect the scratched defect pixels on the same line. The background fluctuation was removed by calculating the differential excitation image, and the difference between pixels was enhanced to strengthen the weak gray jump of scratch defects. However, the enhanced background noise and information are shown in Fig. 9.

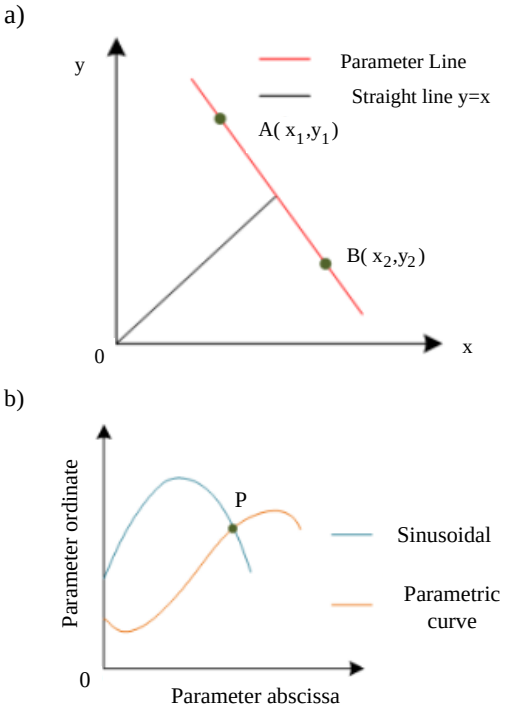

Fig. 8. Hough transform schematic diagram: a) Parameterization of Cartesian coordinate system, b) Intersection of Sine wave in Polat coordinate system

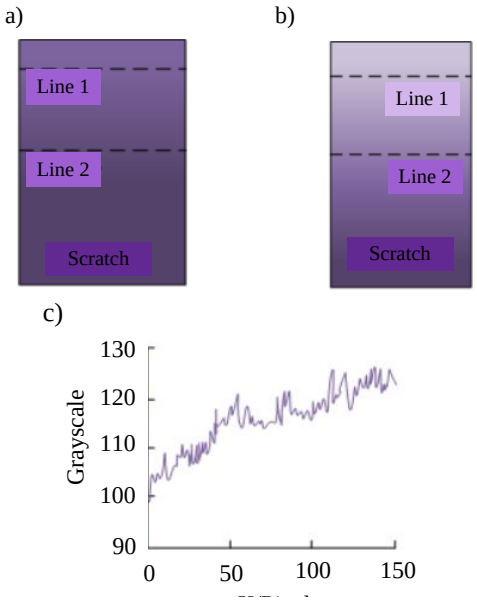

Fig. 9. Original grayscale and its grayscale change: a) original grayscale containing defects, b) calculation results of differential excitation images, c) gray level change of original grayscale without defects

From Fig. 9 (a), it was found that the difference in the original grayscale image of the scratch defect information was small. In Fig. 9 (b), after differential excitation calculation, the grayscale image difference showed a change in brightness. Fig. 9 (c) shows that as the number of pixels increases, the defect information shows a significant change in its grayscale value, with the lowest value below 100, indicating the enhancement effect of the differential excitation algorithm on image grayscale. After that, the gray changes in the differential excitation image were compared, as shown in Fig. 10.

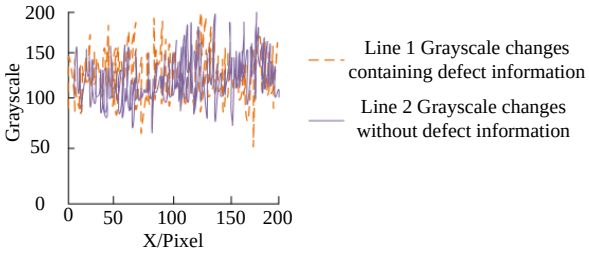

Fig. 10. Grayscale changes of different information in different interaction images

From Fig. 10, it can be observed that the grayscale values of images containing defects varied significantly, with a minimum of 50 and overall higher than the grayscale values of images with defects removed. The grayscale jump enhancement of image defects after differential excitation calculation` led to small differences between the grayscale image of the defect and the background of the grayscale 3D image, which distinguished the grayscale values of the target image and its background, thus clearly detecting the defect information of the sapphire substrate. The grayscale image size of a 4-inch sapphire substrate was 8192 × 8192 with a field of view of 130 mm × 130 mm. Then the Fourier Transform was used to compare high-frequency information, as shown in Fig. 11.

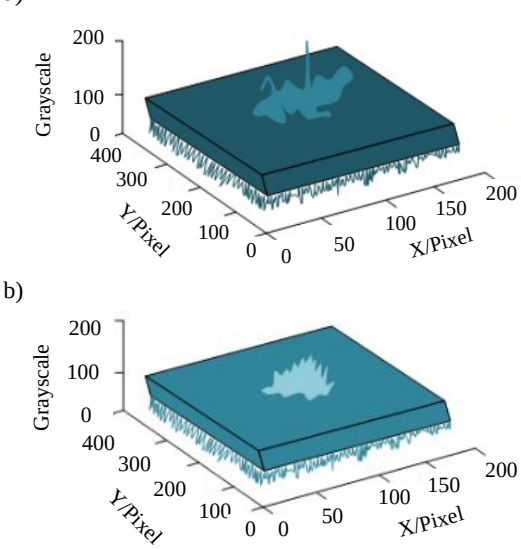

Fig. 11. Differential exception image results of the Fourier Transform: a) SSPOS grayscale three-dimensional image corresponding to Fourier transform amplitude map b) SSOS grayscale three-dimensional image corresponding to Fourier transform amplitude map

From the figure, it can be seen that the direction of the spectral range of scratches in the differential excitation image was perpendicular to the direction of the scratch texture. Fig. 11 (a) shows high-frequency information with a maximum grayscale value of around 200 and contains

less Gaussian noise. Scratch images are the main information of the whole, and their corresponding frequencies are relatively high. In Fig. 11 (b), after Fourier transform, the scratch image information was basically free of Gaussian noise, indicating the ability of Fourier transform to handle noise. Then the spectral range of the scratch image in the region was extracted and the grayscale changes were observed, as shown in Fig. 12.

a)

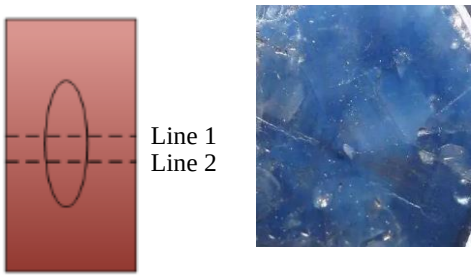

b)

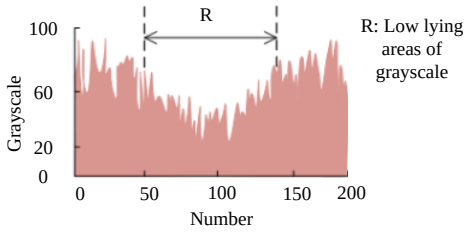

c)

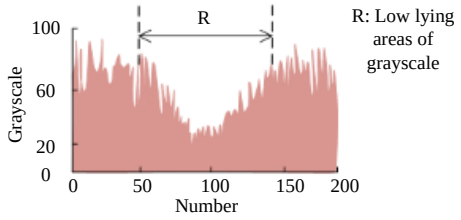

Fig. 12. Background analysis of spectral images: a) amplitude map of differential excitation image after Fourier transform, b) excluding grayscale changes in Line 1, c) excluding grayscale changes in Line 2

It is found from Fig. 12 (a) that the grayscale values in the central region are all low and close to the grayscale of the image boundary. The lowest grayscale value in Fig. 12 (b) was 20, while the lowest grayscale value in Fig. 12 (c) was above 20. This further indicates that the amplitude of the low-frequency Fourier transform was lower than that of the high-frequency transform, corresponding to more high-frequency information, and the scratch information is lower than the surrounding information. Therefore, when segmenting scratch information, the low-lying gray area was first segmented, and then the frequency information was segmented corresponding to the scratch. After the best gray segmentation threshold was obtained, the scratch was segmented and extracted from the image, as shown in Fig. 13.

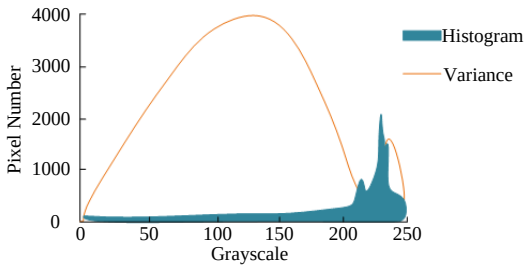

Fig. 13. Grayscale segmentation image

From Fig. 13, it can be observed that the spectral range corresponding to scratches was roughly extracted from the low-lying gray areas. The low-lying areas were within the range of gray values 0-200, and there were fluctuations in the range of gray values 200-250. The variance of pixel count continued to increase in grayscale values from 0 to 100, decreased in grayscale values from 100 to 200, slightly increased in grayscale values around 200 to 230, and continued to decrease around 250. The highest value of variance reached during the entire process was 4000. Then, fine extraction was performed based on the spectral range, using binarization and other processing methods. Finally, the image was constructed using feature enhancement methods for future evaluation of scratch defects. According to the 4-inch sapphire substrate image of 8192 × 8192, which is divided into 16 word images, and the pixel size of each subimage is 250 × 250, calculate the length, the actual length, the total pixel area and the scratch image, and obtain the actual length and width of the whole scratch, as shown in Table 1.

Table 1. Scratch defects in sapphire subsidiaries

Calibration coefficient	0.01663	Average diameter of sample	6109.50 pixel	Average nominal value of sample diameter	101.60 mm
Scratch length		Scratch pixel length	184 pixel	Calculated length of scratches	3.06 mm
Scratch width		Scratch pixel width	7.23 pixel	Scratch calculation width	0.12 mm

It can be seen from Table 1 that the resolution of the detection system used is about 16um. Several sub images of the 4-inch sapphire substrate were calculated and detected, and the calibration coefficient was 0.01663. The average diameter of the sample was 6109.50 pixels, and the average nominal value of the diameter was 101.60 mm. The results showed that the scratch pixel length was 184 pixels, the actual length was 3.06 mm, the scratch pixel width was 7.23 pixels, and the actual width was 0.12 mm. For metal surface defect detection, the VDEDDF algorithm was compared with the

improved YOLOv3 algorithm and BP neural network model in terms of detection performance, as shown in Table 2.

Table 2. Performance and error comparison results of different detection models

Detection performance	The VDEDDF algorithm	Improved YOLOv3 algorithm	BP neural network model
Accuracy(%)	99.86%	89.47%	91.73%
Noise factor(%)	0.04%	0.26%	0.13%
Loss(%)	0%	0.03%	0%
Time(s)	0.009s	0.034s	0.018s
Average error(%)	1.02%	2.26%	1.93%

From Table 2, it can be seen that for the same batch of detection samples, the far-field imaging system has better detection performance, with accuracy, false detection rate, and missed detection rate of 99.86%, 0.04%, and 0%, respectively. Classification network models often suffer from noise interference and loss in performance testing, and the prediction of scratch measurements also reflects the accuracy of the model. The noise factor reflects the surface background in surface defect detection, and the larger the noise, the stronger the interference of the background on defect detection. The lowest noise factor result in this research method is 0.04%. The loss coefficient represents the attention of the detection model to the defect area during the training process. The lower the loss coefficient, the higher the model's attention and ability to detect the object. The loss coefficient value of the research method is consistent with that of the BP neural network model, which is 0%. The average error of the detection object can reflect the detection accuracy of the model for defects. The smaller its value, the stronger the detection performance of the model, which is conducive to the precision production of ultra precision workpieces. Compared with the other two methods, the detection time and average error of the research method are relatively small, at 0.009s and 1.02% respectively, demonstrating the superior performance of the system. Finally, the performance of ultra precision machining methods is compared and analyzed, as shown in Table 3.

From Table 3, it can be concluded that the telecentric imaging system based on visual difference algorithm and Fourier transform has a higher analysis of precision components. The accuracy, sensitivity, and specificity are 99.86%, 99.99%, and 0%, respectively, indicating the superiority of its ultra precision machining technology. In a word, the scratch texture and background noise texture of the original image were enhanced by using the visual difference operator. In order to extract the image with only scratch, twice the Fourier Transform was used to extract the scratch spectrum range, and then gray segmentation was used to extract the scratch range and the scratch defect image. Binary image and line detection were used to extract the binary image and calculate the actual size of the scratch defect.

Table 3. Analysis results of surface detection of components using different ultra precision machining techniques

Method	Accuracy (%)	Sensitivity (%)	Specificity (%)
Visual inspection processing technology [26]	88.34%	88.94%	11.06%
The Processing Technology of K-means Algorithm [27]	89.97%	89.76%	10.24%
Deep Recurrent Neural Networks Algorithm [28]	95.12%	91.64%	8.36%
The VDEDDF algorithm	99.86%	99.99%	0%

5. CONCLUSION

For the detection system of precision machined components, the detection of the upper and lower surfaces of single-sided polished optical components based on machine vision detection technology is studied. The scratch marks on the super smooth upper surface of the substrate surface of the sapphire substrate are used as the detection object of component defects. Firstly, a telecentric bright field imaging system based on coaxial incidence is proposed for different light effects, which can detect the upper and lower surfaces with different properties. Due to the inconsistency of the defect location, the detection and location image of the defect location needs the change of gray value to distinguish it, so as to extract the scratch defect information which is different from the surrounding information and background noise information; According to the human visual characteristics, a weak information extraction algorithm based on visual differential excitation and double discrete the Fourier Transform is proposed, which can accurately extract and strengthen the defect texture information; The results showed that the average diameter of the sample was 6109.5 pixel, the average nominal value of the diameter was 101.6 mm, the scratch pixel length was 184 pixel, the actual length was 3.06 mm, the scratch pixel width was 7.23 pixel, the actual width was 0.1202 mm. Finally, the superior performance of scratch defect detection technology based on weak information of visual differential excitation and double discrete the Fourier Transform was proved. However, the research still lacks data support for the actual industrial processing component testing, as well as the comparative data of different types of components, so the application research and improvement should be carried out in the follow-up.

Source of funding: *This research received no external funding.*

Declaration of competing interest: *The author declares no conflict of interest.*

REFERENCES

1. Tang B, Chen L, Sun W, Lin Z. Review of surface defect detection of steel products based on machine vision. IET Image Processing. 2023;17(14):303-322. https://doi.org/10.1049/IPR2.12647.
2. Singh SA, Desai KA. Automated surface defect detection framework using machine vision and convolutional neural networks. Journal of Intelligent Manufacturing. 2023;34(4):1995-2011. https://doi.org/10.1007/S10845-021-01878-W.
3. Doshvarpassand S, Wang X, Zhao X. Sub-surface metal loss defect detection using cold thermography and dynamic reference reconstruction (DRR). Structural Health Monitoring 2022;21(2):354-369. https://doi.org/10.1177/1475921721999599.
4. Xu L, Hu J. A method of defect depth recognition in active infrared thermography based on GRU networks. Applied Sciences. 2021;11(14):63-87. https://doi.org/10.3390/app11146387.
5. Mao Y, Wang S, Yu S, Zhao J. Automatic image detection of multi-type surface defects on wind turbine blades based on cascade deep learning network. Intelligent Data Analysis. 2021;25(2):463-482. https://doi.org/10.3233/IDA-205143.
6. Duan H, Wei J, Qi L, Wang X, Liu Y, Yao M. Longitudinal crack detection approach based on principal component analysis and support vector machine for slab continuous casting. Steel Research International. 2021;92(10):168-178. https://doi.org/10.1002/srin.202100168.
7. Kang SH, Kang M, Kang LH. Defect detection on the curved surface of a wind turbine blade using piezoelectric flexible line sensors. Structural Health Monitoring. 2022;21(3):1207-1217. https://doi.org/10.1177/14759217211026192.
8. Hua S, Li B, Shu L, Jiang P, Cheng S. Defect detection method using laser vision with model-based segmentation for laser brazing welds on car body surface. Measurement. 2021;178(1):1-13. https://doi.org/10.1016/j.measurement.2021.109370.
9. Preeyanka N, Sarkar M. Probing how various metal ions interact with the surface of QDs: Implication of the interaction event on the photophysics of QDs. Langmuir. 2021;37(23):6995-7007. https://doi.org/10.1021/acs.langmuir.1c00548.
10. Ai Y, Zhang Y, Cao X, Zhang W. A defect detection method for the surface of metal materials based on an adaptive ultrasound pulse excitation device and infrared thermal imaging technology. Complexity. 2021;2021(7):1-9. https://doi.org/10.1155/2021/8199013.
11. Zhao H, Yang Z, Li J. Detection of metal surface defects based on YOLOv4 algorithm. Journal of Physics: Conference Series 2021; 1907(1): 012-043. https://doi.org/10.1088/1742-6596/1907/1/012043.
12. Yu X, Wang K, Wang S. Research on image recognition of building wall design defects based on partial differential equation. Advances in Mathematical Physics. 2021;2021(3):1-10. https://doi.org/10.1155/2021/1229660.
13. Aydin I, Akin E, Karakose M. Defect classification based on deep features for railway tracks in sustainable transportation. Applied Soft Computing. 2021;111(7): 107706-107720. https://doi.org/10.1016/j.asoc.2021.107706.
14. Wang H, Gao C, Ling Y. A deep learning-based method for aluminum foil-surface defect recognition. International Journal of Information and Communication Technology. 2021;19(3):231-241. https://doi.org/10.1504/IJICT.2021.117532.
15. Zhuang J, Peng Q, Wu F, Guo B. Multi-component attention-based convolution network for color difference recognition with wavelet entropy strategy. Advanced Engineering Informatics. 2022;2022(52): 613-626. https://doi.org/10.1016/j.aei.2022.101603.
16. Zachman MJ, Yang Z, Du Y, Chi M. Robust atomic-resolution imaging of lithium in battery materials by center-of-mass scanning transmission electron microscopy. ACS Nano. 2022;16(1):1358-1367. https://doi.org/10.1021/acsnano.1c09374.
17. Chen Y, Shu Y, Li X, Xiong C, Cao S, Wen X, Xie Z. Research on detection algorithm of lithium battery surface defects based on embedded machine vision. Journal of Intelligent & Fuzzy Systems: Applications in Engineering and Technology. 2021;41(3):4327-4335. https://doi.org/10.3233/JIFS-189693.
18. Danjuma MU, Yusuf B, Yusuf I. Reliability, availability, maintainability, and dependability analysis of cold standby series-parallel system. Journal of Computational and Cognitive Engineering. 2022; 1(4):193-200. https://doi.org/10.47852/bonviewJCCE2202144.
19. Rabha D, Biswas S, Chamuah N, Chamuah N, Mandal M, Nath P. Wide-field multi-modal microscopic imaging using smartphone. Opticsand Lasers in Engineering. 2021;137(2):431-438. https://doi.org/10.1016/j.optlaseng.2020.106343.
20. Lu L, Li J, Shu Y, Sun J, Zhou J, Ylam E, Chen Q, Zou C. Hybrid brightfield and darkfield transport of intensity approach for high-throughput quantitative phase microscopy. Advanced Photonics. 2022;4(5): 15-26. https://doi.org/10.1117/1.AP.4.5.056002.
21. Chen TB, Zeng XF, Zhang ZY, Zhang F, Bai YY, Zhang XJ. REM: A simplified revised entropy image reconstruction for photonics integrated interference imaging system. Optics Communications. 2021; 501(1):11-16. https://doi.org/10.1016/j.optcom.2021.127341.
22. Schrimpf M, Graefe PA, Kaczyna AE, Vorholt AJ, Leitner W. Measuring droplet sizes generated by 3D-printed stirrers in a lean gas-liquid-liquid system using borescopy. Industrial & Engineering Chemistry Research. 2022;61(7):2701-2713. https://doi.org/10.1021/acs.iecr.1c03707.
23. Yue Y, Sun M, Li X, Liu J, Lu Y, Chen J, Peng Y, Maraj M, Zhang J, Sun W. Quality improvement mechanism of sputtered AlN films on sapphire substrates with high-miscut-angles along different directions. Cryst Eng Comm. 2021;23(39):6871-6878. https://doi.org/10.1039/D1CE00654A.
24. Chen J, Wang G, Meng J, Cheng Y, Yin Z, Yan T, Huang J, Zhang S, Wu J, Zhang X. Low-temperature direct growth of few-layer hexagonal boron nitride on catalyst-free sapphire substrates. ACS Applied Materials&Interfaces. 2022;14(5):7004-7011. https://doi.org/10.1021/ACSAMI.1C22626.
25. Zhang W, Lei H, Liu W, Zhang Z. Effect of the carboxyl group number of the complexing agent on

polishing performance of alumina slurry in sapphire CMP. Ceramics International. 2023;49(9):13687-13697. https://doi.org/10.1016/j.ceramint.2022.12.246.
26. Tang B, Chen L, Sun ZK. Review of surface defect detection of steel products based on machine vision. IET Image Processing. 2023;17(2):303-322. https://doi.org/10.1049/ipr2.12647.
27. Zhang X, Han X, Fu C. Comparison of object region segmentation algorithms of PCB defect detection. Traitement du Signal. 2023;40(2):797-802. https://doi.org/10.18280/ts.400241.
28. Silenzi A, Castorani V, Tomassini S, Falcionelli N, Contardo P, Bonci A, Dragoni AF, Sernani P. Quality control of carbon look components via surface defect classification with deep neural networks. Sensors. 2023;23(17):1-18. https://doi.org/10.3390/s23177607.

Zhuolin LI obtained a doctoral degree in Optical Engineering from Changchun University of Technology in 2017. She received her Bachelor and Master degree from same university and graduated in 2009 and 2012. Her research work is mainly focused on Optical ultra-precision manufacturing technology, Science and technology innovation education.
She worked as a research assistant in the Hong Kong State Key Laboratory in Ultra-precision Machining Technology from 2013 to 2014. Then she is engaged in teaching in high school attached to Northeast Normal University. Since 2022, she has worked as a teaching and research staff of Jilin Provincial Institute of Education.
Has published more than 10 academic articles, participated in 5 scientific research projects, and other academic research and achievements.
e-mail: zhuolin77772023@163.com